Co-evaporated Perovskites with Fermi Levels Enable Highly Performing p-i-n Perovskite Solar Cells

Jia Li, Herlina Arianita Dewi, Hao Wang, Jiashang Zhao, Nidhi Tiwari, Natalia Yantara, Tadas Malinauskas, Vytautas Getautis, Tom J. Savenije, Nripan Mathews, [*] Subodh Mhaisalkar, [*] Annalisa Bruno [*]

Dr. Jia Li, Dr. Herlina Arianita Dewi, Dr. Hao Wang, Dr. Nidhi Tiwari, Dr. Natalia Yantara, Prof. Nripan Mathews, Prof. Subodh Mhaisalkar, Dr. Annalisa Bruno,
Energy Research Institute @ NTU (ERI@N), Nanyang Technological University, 637553, Singapore
E-mail: (annalisa@ntu.edu.sg, nripan@ ntu.edu.sg; subodh@ntu.edu.sg)

Dr. Jiashang Zhao, Prof. Tom J. Savenije,
Department of Chemical Engineering, Delft University of Technology, 2629 HZ Delft, The Netherlands

Dr. Tadas Malinauskas, Prof. Vytautas Getautis,
Department of Organic Chemistry, Kaunas University of Technology, Kaunas LT-50254, Lithuania.

Prof. Nripan Mathews, Prof. Subodh Mhaisalkar,
School of Materials Science & Engineering, Nanyang Technological University, Singapore, 639798.

Abstract

Recent progress of vapor-deposited perovskite solar cells (PSCs) has proven the feasibility of this deposition method in achieving promising photovoltaic devices. Here we probe, for the first time, the versatility of the co-evaporation process in creating perovskite layers

1

customizable for different device architectures. We create a gradient of composition within the perovskite films by tuning the background chamber pressure during the growth process. This method leads to co-evaporated $MAPbI_3$ film with graded Fermi levels across the thickenss. Here we prove that this growth process is beneficial for p-i-n PSCs as can guarantee a favorable energy alignment at the charge selective interfaces.

Co-evaporated p-i-n PSCs, with different hole transporting layers, consistently achieved power conversion efficiency (PCE) over 20% with a champion value of 20.6%, one of the highest reported to date. The scaled-up p-i-n PSCs, with active areas of 1 and 1.96 cm^2, achieved the record PCEs of 19.1% and 17.2%, respectively while the flexible PSCs reached a PCE of 19.3%. Unencapsulated PSCs demonstrate remarkable long-term stability, retaining ~90% of their initial PCE when stored in ambient for 1000 hours. These PSCs also preserve over 80% of their initial PCE after 500 hours of thermal aging at 85 °C.

Introduction

In the last decade, organic-inorganic metal halide perovskites (ABX_3) have revolutionized the field of photovoltaic due to their excellent optoelectronic properties [1, 2] such as high defect tolerance [3], long carrier diffusion lengths [4-6], and ambipolar carrier transport [7], enabling state-of-the-art perovskite solar cells (PSCs) to achieve certified power conversion efficiency (PCE) of 25.5% [8] over small area devices and over 18% for perovskite mini-modules [9, 10].

The rapid progress of PSCs is strongly related to the improvements in the perovskite composition and process engineering quality as well as the development of device architecture facilitating efficient charge extraction. While perovskite fabrication typically involves solution-based processing, such as spin-coating [11-15] and coating methods, [16, 17] [18] [19], vapor-based deposition methods represent an attractive processing alternative obtaining high-quality and uniform thin films required for highly efficient PSCs [9, 10, 20-22] and optoelectronic devices. [23] This is further compounded by promising reports on vapor-deposited $MAPbI_3$ PSCs with PCEs

over 20% in small area devices (<<1 cm^2) [9, 21, 24, 25] and PCEs of up to 18% [26, 27] for PSCs based on co-evaporated multi-cation perovskites. Not only does the vapor process offer full and uniform coverage of perovskite films on different substrates such as flexible and textured ones [28, 29] , but also the intrinsic additivity of the dry process due to the elimination of solvents through this process makes it ideal process approach for the development of perovskite/perovskite tandem solar cells [30]. Co-evaporated PSCs have also recently demonstrated a remarkable intrinsic long-term stability thanks to the un-straitened perovskite films grown by co-evaporation.[31] The excellent scalability of this technique results in co-evaporated perovskite mini-modules achieving PCEs well above 18% paving the way for PSC commercialization. [20] [10]

Although most of the highly efficient PSCs are based on the n-i-p structure [32-34], the advantages provided by the p-i-n configuration such as a reduction in hysteresis and processing complexity as well as an increase in cost-effectiveness, are rapidly gaining the attention of the scientific community [35, 36]. Moreover, the prospect of achieving high transparency in p-i-n PSCs is also attractive for integration in high-performing perovskite/silicon tandem solar cells [29, 37, 38] and in urban contexts [39]. To date, there have been few reports of highly efficient, vapor-deposited

p-i-n PSCs as summarized in **Table S1** and just two with PCEs achieving 20%. [40, 41] Moreover,

to the best of our knowledge, the record PCE of a large area (1 cm^2) co-evaporated PSC are 18.1% [42] and 19% [9] for the p-i-n and n-i-p architecture respectively. The state of the art for the large area thermally evaporated PSCs together with their main characteristics are summarized in **Table 1**.

One of the key factors driving the performances of the p-i-n PSCs architectures is that the photo-generated carriers, which tend to be generated near the hole selective contact, have to move a long way across the perovskite film until they reach the electron selective layers. [43] An interesting approach to facilitate charge transport in solution-processed PSCs is the creation of

a graded perovskite layer, [43-46] by either varying the perovskite composition, and in turn the bandgap, or by external [46, 47] or self-doping [48, 49]. However, the main limitation of this method for the spin-coating approach is the imprecise control over dopant diffusion depth inside the film. [43, 46]

In this work, we show the versatility of the co-evaporation process in creating controlled and graded perovskite layers customizable for different device architectures without introducing any extra layer or passivation process. Indeed, we prove that graded Fermi levels in $MAPbI_3$ film can be achieved by continuously varying the stoichiometry of $MAPbI_3$ during the evaporation process. This condition can be achieved by varying the background pressure during the whole evaporation process. We have studied the crystallinity, composition, and electrical properties of co-evaporated $MAPbI_3$ films of different thicknesses by scanning electron microscopy (SEM), UV-Vis absorption, photoluminescence (PL), grazing incidence wide-angle XRD (GIWAX), X-ray diffraction (XRD), X-ray photoelectron spectroscopy (XPS), Ultra-violet photoelectron spectroscopy (UPS) and time-resolved microwave-conductivity measurements (TRMC). The different investigative techniques have consistently shown that the PbI_2: MAI ratio progressively increases with the deposition time, resulting in an increasingly n-type perovskite film with higher Fermi levels as the deposition progresses. The variation of the Fermi level results in a continuous band bending inside perovskite film in the same direction of the band alignment in the p-i-n structure which helps the electron transport and that maximizes the performance of the PSCs. At the same time, we also show here that the same gradient structure is not favorable for n-i-p PSCs, where the band alignment should indeed be opposite.

Herein, we further prove how the co-evaporation process can be adapted to different p-i-n and n-i-p architectures. Indeed, by tuning the co-evaporation conditions we demonstrate small-area p-i-n PSCs based on different electron and hole-transporting materials consistently achieving PCEs above 20%, while the same $MAPbI_3$ growing conditions are not favorable for n-i-p PSCs.

The champion PSCs employing MeO-2PACz as hole transport layer (HTL), reached a PCE of 20.6%. PSCs with active areas of 1 cm^2 and 1.96 cm^2 reached PCEs as high as 19.1% and 17.2% respectively. Flexible p-i-n PSCs, adopting the same device architecture, have also shown PCEs of 19.3% with a fill factor exceeding 80%.

Moreover, the unencapsulated PSCs demonstrated remarkable stability, retaining over 90% of the initial PCEs despite storing in ambient with 30% relative humidity (RH) for more than 1000 hours. Retention of over 80% of initial PCE after 500 hours of thermal aging at 85 °C in the absence of any encapsulation or protection layers further attests to the long-term stability of these devices.

Table 1. State-of-the-art high-performing large area thermal-evaporated PSCs.

Architecture	Structure	Deposition Method	Area (cm^2)	PCE (%)	Ref
n-i-p	FTO/SnO$_2$/PCBM/MAPbI$_3$/Spiro-OMeTAD/Au	Co-evaporation	1	19.0	[9]
			4	16.6	
n-i-p	FTO/TiO$_2$/CsPbBr$_3$/Spiro-OMeTAD/Au	Co-evaporation	1	5.37	[50]
n-i-p	FTO/TiO$_2$/MAPbI$_3$/Spiro-OMeTAD/Au	Layer-by layer evaporation	0.8	15.9	[51]
n-i-p	ITO/C$_{60}$-PhIm/MAPbI$_3$/F$_6$-TCNNQ/Au	Co-evaporation	0.85	15.0	[21]
p-i-n	ITO/PTAA/MAPbI$_3$/C$_{60}$/BCP/Ag	Layer-by layer evaporation	1	18.1	[42]
p-i-n	**ITO/Spiro-TTB/MAPbI$_3$/PCBM/BCP/Ag**	**Co-evaporation**	**1**	**19.1**	**This work**
p-i-n	**ITO/Spiro-TTB/MAPbI$_3$/PCBM/BCP/Ag**	**Co-evaporation**	**2**	**17.2**	**This work**

Results and discussion
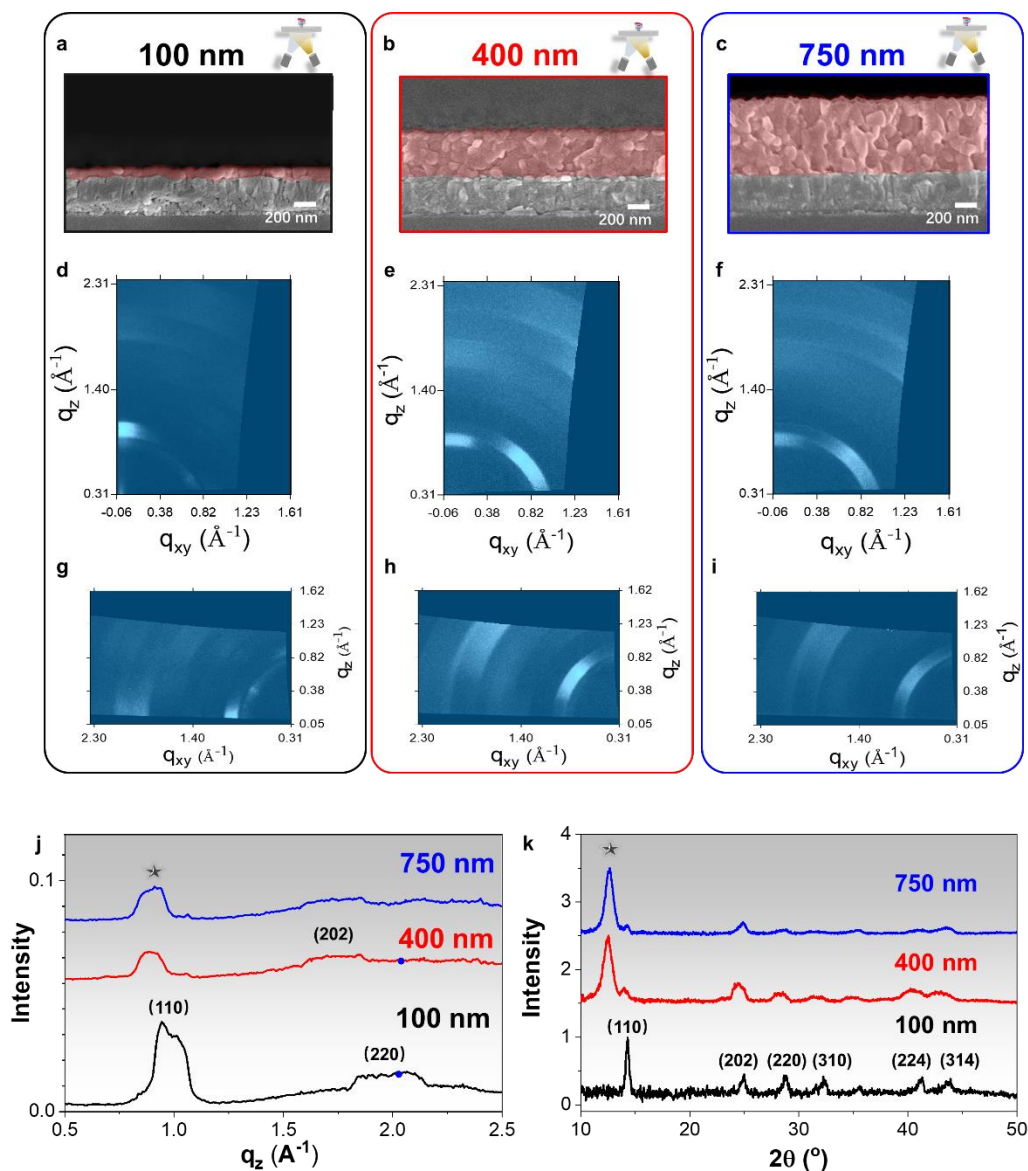
Figure 1. Crystalline structures of co-evaporated MAPbI₃ thin films with different thicknesses. Cross-sectional SEM images of the **a.**100 nm, **b.** 400 nm, and **c.** 750 nm co-evaporated MAPbI₃ thin films on FTO glass. Out-of-plane and in-plane GIWAX patterns of the 100 nm (**d.** and **g.**), 400 nm (**e.** and **h.**), and 750 nm (**f.** and **i.**) co-evaporated MAPbI₃ thin films. **j.** Out-of-plane Bragg intensities integrated over the different diffraction angles are plotted as a function of the q_z range investigated. **k.** XRD patterns of perovskite films at the incident angle of 0.5 degrees (the star represents PbI₂ peak).

Most of the optical, morphological, and structural properties of the MAPbI₃, during the co-evaporation process, are usually controlled by fixing the main sublimation parameters such as the sources' temperatures [9, 52], the substrate temperature [40, 53], and the chamber background

pressure [54, 55]. In this work, instead, we propose an alternative way to control the $MAPbI_3$ deposition process where the chamber background pressure is slowly decreased during the whole perovskite growth. Since the background pressure is mainly related to the low-molecular-weight MAI partial pressure, its decrease will mainly affect the MAI deposition on the substrate. Here, the $MAPbI_3$ was co-evaporated by gradually reducing the chamber background pressure from 1×10^{-5} to 1.2×10^{-6} torr, **Figure S1**, while keeping the evaporation temperatures of PbI_2 and MAI constant at ~260 °C and ~100 °C, respectively during the entire process.

To understand the growth mechanism of the co-evaporated $MAPbI_3$ films during this process, we have probed the structural, electrical, and spectroscopic properties of three $MAPbI_3$ films with different thicknesses. The resulting films' thicknesses were controlled by varying the total growth duration.

The cross-sectional SEM images showed $MAPbI_3$ thin films with different thicknesses of 100 nm, 400nm, and 750 nm, **Figure 1a**, **Figure 1b**, and **Figure 1c**, revealed similar morphology and grain average sizes of approximately 130 nm, **Figure S2**. The three films also demonstrate consistent optical properties with varying thicknesses, **Figure S3**.

We further investigate the crystallinity and structural properties of these films by GIWAX and XRD. The out-of-plane and in-plane GIWAX measurements were carried out with an incidence angle of 0.2° which guarantees a penetration depth of roughly 4 nm [56], (**Figure 1d** to **Figure 1i**). For clarity, the results have been summarized in **Figure 1j** where the Bragg peak intensities integrated over the whole arch (range of diffraction angles) and are reported as a function of the q_z range investigated. The GIWAX patterns highlight the different compositions and orientations for the three thicknesses. The 100 nm thick $MAPbI_3$ film shows an out-of-plane diffraction pattern dominated by the well-localized Bragg pick at $q_z = 1$ Å^{-1}, **Figure 1d**, indicating that the (110) $MAPbI_3$ planes are well-oriented, perpendicular to the substrate surface. Moreover, a small Bragg peak at $q_z = 0.91$ Å^{-1} in **Figure 1d** shows that the slight PbI_2 excess

present in the film does not exhibit any preferred orientation, as revealed by the Bragg peak intensity distributed along the whole arch in the in-plane GIWAX patterns in **Figure 1g**.

These results are consistent with the XRD spectra taken with an incident angle of 0.5°, **Figure 1h**, which shows that the thin 100 nm film exhibits the main peak at 14.1° corresponding to (110) orientation of $MAPbI_3$ with a slight excess of PbI_2.

On the other hand, the 400 nm and 750 nm $MAPbI_3$ films reveal different specific major characteristics in both the out-of-plane and the in-plane GIWAX measurements, **Figure 1e** and **Figure 1h** for the 400 nm film and **Figure 1f** and **Figure 1i** for the 750 nm respectively. In both the 400 nm and 750 nm films, the Bragg peaks at $q_z=1$ $Å^{-1}$ show the strongest intensities along the extended arc segments indicating that $MAPbI_3$ crystal domains orientation is titled with respect to the substrate surface and not perpendicular to it, unlike the 100 nm film. Moreover, in **Figure 1e** and **Figure 1f**, the Bragg peaks at $q_z = 1.73$ A^{-1} become more dominant, indicative of the crystallization orientation along the (202) planes for the 400 and 750 nm $MAPbI_3$ films. Furthermore, a well-defined PbI_2 Bragg peak along the z-axis at $q=0.91$ $Å^{-1}$ can be detected in the out-of-plane plot which indicates that in this case the PbI_2 is well oriented with the (001) plane perpendicular to the substrates.

The GIWAX results are in good agreement with the XRD diffraction patterns obtained with a 0.5° incident angle shown in **Figure 1k**. Indeed the 400 nm and 750 nm thick samples present a small peak at $14.1^{\circ,}$ corresponding to the $MAPbI_3$ (110) orientation, while the more pronounced peaks at 24.5 and 12.6°, are assigned to $MAPbI_3$ (202) orientation and (001) orientation of PbI_2, respectively. The XRD patterns of films with different thickness (*i.e.:* 40 nm, 200 nm, and 500 nm) are also shown in **Figure S4**, these thin films also show that as the perovskite films grow thicker, the PbI_2 to perovskite ratio increases, consistently to what has been observed for the other thicknesses.
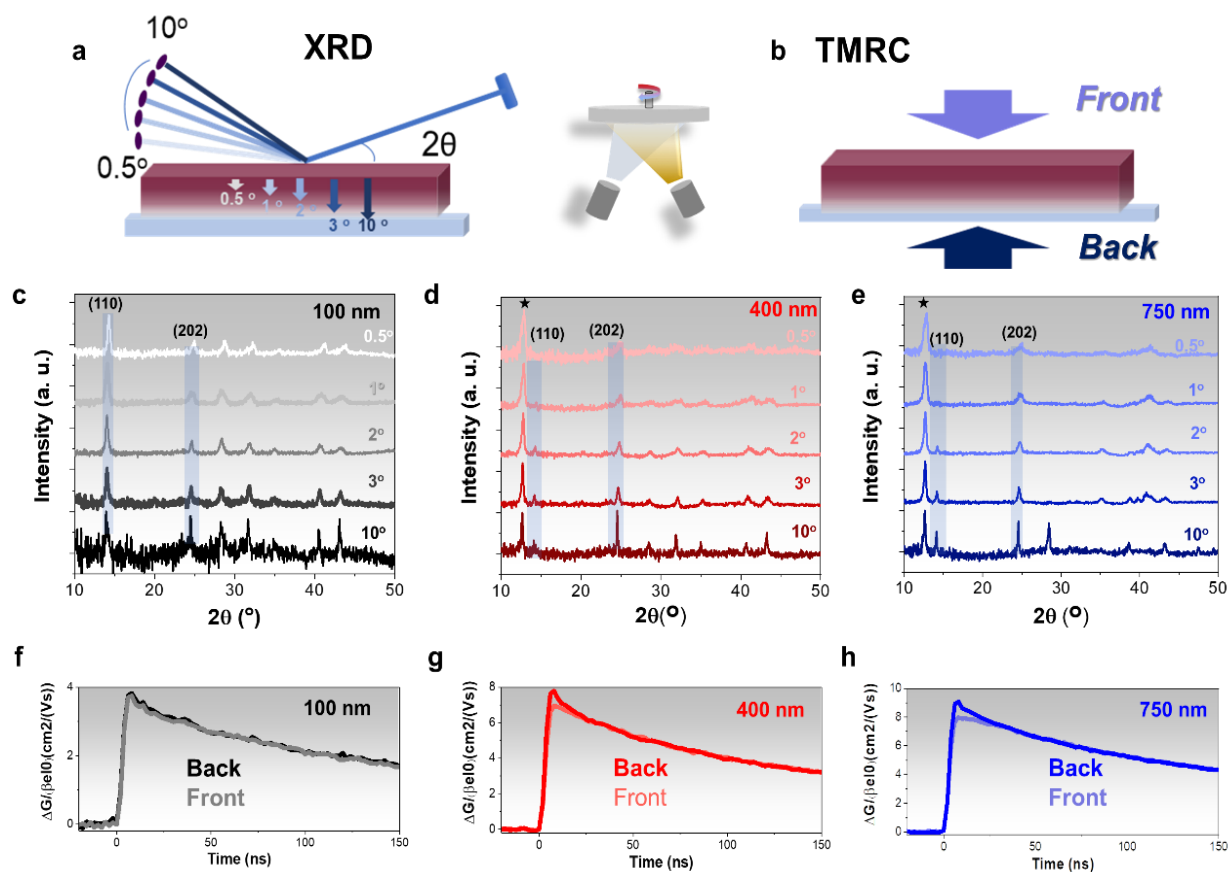
Figure 2. Gradient composition of the MAPbI₃ thin film. a. angle-dependent XRD measurements schematic **b.** Time-resolved microwave conductivity measurement (TMRC) schematic with excitation from the front and back of the perovskite film. XRD patterns with incident angles ranging from 0.5 to 10º for the **c.** 100 nm, **d.** 400 nm and **e.** 750 nm co-evaporated MAPbI₃ films. TMRC decay curves of the **f.** 100 nm, **g.** 400 nm and **h.** 750 nm co-evaporated MAPbI₃ films with front and back illumination.

GIWAX measurements highlight the differences in orientations and composition on the top surfaces of the three films investigated. To correlate these orientations to the compositional variations across the film thickness, we measured the XRD spectra with incident angles varying from 0.5º to 10º to be able to investigate compositional differences at the various depths. Indeed, as shown in **Figure 2a**, increasing the incident angle the penetration depth increases allowing investigation into the deeper regions of the film *i.e.,* probing the material from the top surface to the bottom (**Figure S5** and **Table S2**), and the resulting XRD patterns are the integrated signal over the whole penetration depth.

In the 100 nm film, the XRD patterns do not vary significantly on increasing the incident angle, suggesting a homogeneous perovskite composition across the film thickness (**Figure 2c**). However, in the 400 and 750 nm films, the $MAPbI_3$ peaks at (110) and (202) become increasingly more pronounced (relative to PbI_2), with increasing incident angle (**Figure 2d**-**Figure 2e**). These data indicate a gradual increase of PbI_2 content from the bottom to the top for the 400 and 750 nm $MAPbI_3$ films.

Moreover, XPS measurements on the three $MAPbI_3$ films deposited on ITO showed that the iodine to lead ratio (I: Pb) on the top surface varied from 2.7±0.3 to 2.2±0.3 when the film thickness is increased from 100 nm to 750 nm, **Figure S6**, and **Table S3**. These results agree with the higher PbI_2 contents detected at the surface from the GWAX and XRD measurements. Moreover, all the spectra have been fitted using a synthetic Voigt peak shape function together with Shirly background.[57] The shift of the peaks with increasing the film thickness is neglectable, demonstrating that surface photovoltage effects are not affecting the measurements. This compositional gradient is created during the entire deposition process as the deposition rate of MAI is significantly affected by chamber pressure and the substrate temperature. [53, 55] Indeed, by keeping the PbI_2 and MAI temperatures constant during the evaporation of MAI can be slowly reduced as the chamber pressure decreases during the evaporation process. Therefore, graded $MAPbI_3$ film is formed due to MAI deficiency during the growth process. As the film grows thicker, the top surface becomes increasingly PbI_2-rich and the difference in precursor stoichiometry between the top and bottom regions of the perovskite film becomes larger. This hypothesis is further verified by time-resolved microwave conductivity (TRMC) experiments using an excitation wavelength of 300 nm corresponding with a penetration depth of less than 100 nm. [58] The excitation side is illustrated in **Figure 2b**, while **Figure 2f** to **2h** show the different time-resolved traces as measured from the front-side (FS, perovskite side) and backside (BS, quartz side) of the 100, 400, and 750 nm films, respectively. For all samples, a fast rise of the photo-conductance is observed due to the formation of excess, mobile carriers.

The rising signal size with layer thickness is directly related to the increased absorption. In **Figure S7** we also show the TRMC traces obtained on excitation at 500 nm. The signal amplitudes, corrected for the number of absorbed photons, are just over 8 cm^2/Vs independent of the perovskite film thickness. Assuming a charge carrier yield of unity, the value presented here is comparable to previously reported mobility values found for evaporated MAPbI$_3$ layers. [21, 58] Interestingly, while the FS and BS traces for the 100 nm sample in **Figure 2f** are nearly identical, this is not the case for the thicker samples. The initial peak values of the FS and BS signals are significantly different for both the 400 nm and the 750 nm samples with overlapping of the trace signals noted after ~40 ns.

The observed trends are consistent with the presence of PbI$_2$ in the top surfaces for the 400 and 750 nm samples. This is accrued to the strong light-absorbing capability of PbI$_2$ at the excitation wavelength of 300 nm, despite the smaller charge carrier mobility as compared to MAPbI$_3$ [59]. Consequently, the partial absorption of the incident light from the PbI$_2$ carriers leads to the reduced peak photo-conductance of the FS signal, (**Figure 2f**-**Figure 2g**), as observed in previously investigated films containing an excess of PbI$_2$. [60] Rapid charge transfer from PbI$_2$ (wider band-gap) to MAPbI$_3$ (smaller band-gap) eventually results in a signal identical to BS signals.

Moreover, the TRMC traces at longer timescales, **Figure S7** and **Table S4**, reveal substantially longer charge carrier lifetimes with increasing film thickness. We attribute the increase in a lifetime to the passivation of defects by the excess PbI$_2$, which is in agreement with the previously reported results.[59] Hence, we conclude that the variation in perovskite layer composition with the film thickness heavily affects the electronic properties as evidenced by the TRMC measurements.
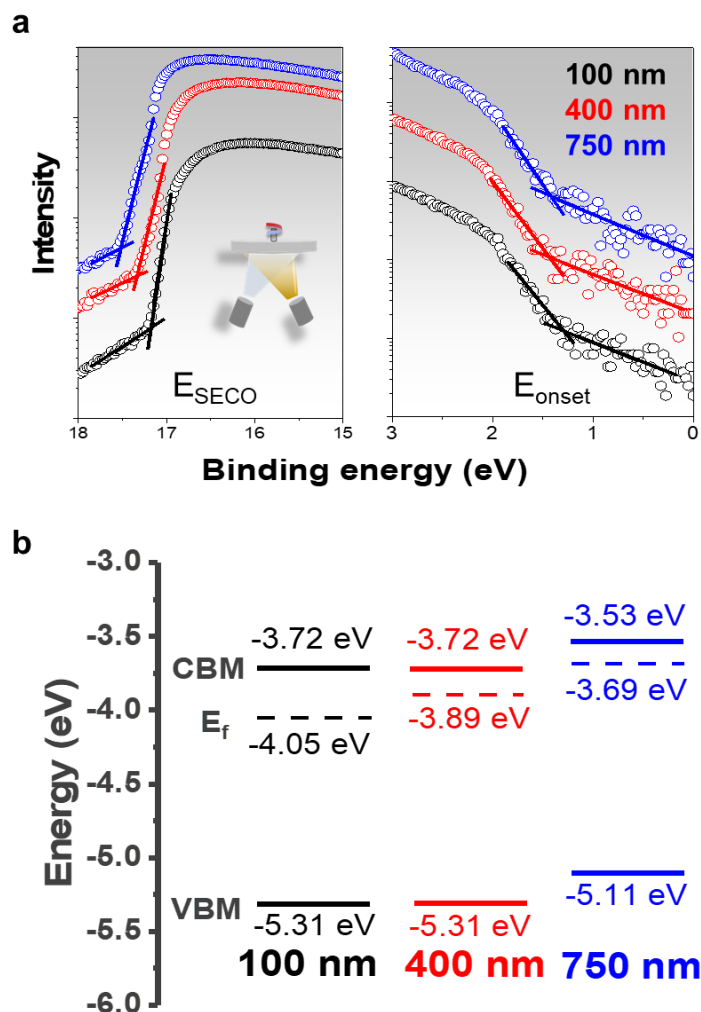
Figure 3. Ultraviolet photoelectron spectroscopy of MAPbI₃ thin films. a. UPS spectra in the energy range between 18-15 eV and 3-0 eV and **b.** schematic energy-level diagrams and the band positions for the MAPbI₃ thin films with different thicknesses.

In agreement with the previous results, UPS measurements on the films with variable thicknesses, **Figure 3a**, show the gradual change in electronic properties on modifying the perovskite film composition. The UPS spectrum shifts to higher energies as the film thickness increases from 100 to 750 nm, indicating a rise in Fermi level (E_F), **Figure 3a**. The Fermi levels can be calculated from the formula $E_F = 21.22 - E_{SECO}$, where E_{SECO} is the secondary electron cut-off energy, obtained as the value of the intersection of the two linear fitting curves, **Figure 3a** left. For the 100 nm, 400 nm, and 750 nm MAPbI₃ films the Fermi level positions have been calculated to be -4.05, -3.89, and -3.69 eV, respectively, **Figure 3b**. The valence band maximum can be calculated from the formula $E_{VBM} = 21.22 - (E_{SECO} - E_{onset})$, where E_{onset}

is the onset electron energy, obtained as the intersection of the two linear fitting curves, **Figure 3a** right. E_{onset} refers to the energy separation between the Fermi level and the valence band maximum. For the 100 nm, 400 nm and 750 nm MAPbI$_3$ films the E_{VBM} have been calculated to be -5.31, -5.31, and -5.11 eV, respectively. By adding these E_{VBM} values to the bandgaps obtained from the absorption spectra in **Figure S2** the positions of the conduction bands for the 100 nm, 400 nm, and 750 nm resulted to be -3.72, -3.72, and -3.53 eV respectively in **Figure 3b**. [61, 62] All energies in **Figure 3b** are referenced to the vacuum level. On the other hand, the positions of the conduction band edge remain similar, indicating increasing n-type doping from the bottom to the top side of the films.As a conseguence, The 400 nm and 750 nm MAPbI$_3$ films are more n-type doped compared to the 100 nm ones .The Fermi level variations noted can be assigned to changes in MAI concentration during the film growth process, where MAI deficiency (excess of PbI$_2$) leads to efficient n-type doping of the perovskite films as reported previously in spin-coated films.[49, 63]
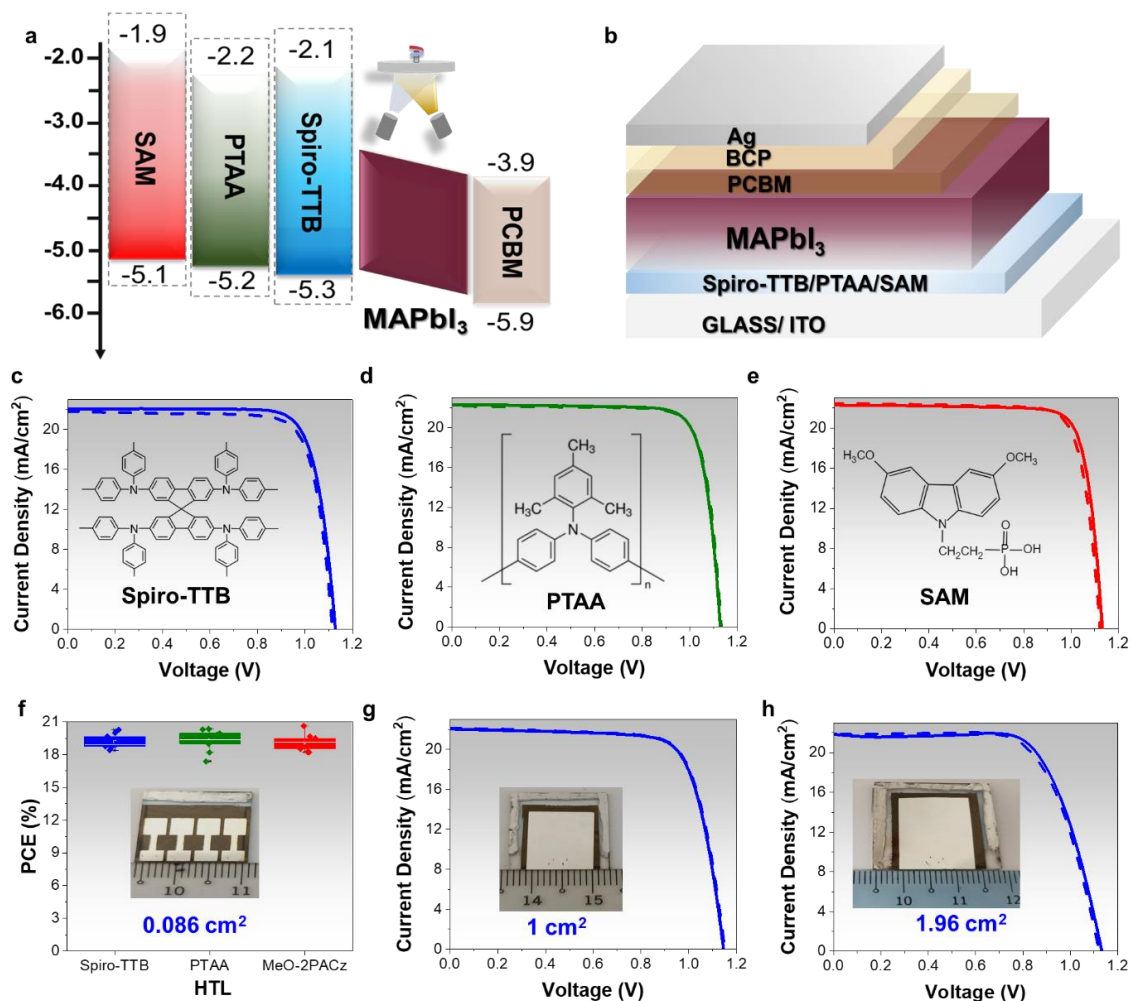
Figure 4. Co-evaporated MAPbI$_3$ p-i-n PSCs. a. Band alignment of the different hole transporting layers, and band bending in perovskite film, **b.** p-i-n PSCs device structure. J-V curves of champion PSCs based on different HTLs: **c.** Spiro-TTB, **d.** PTAA, **e.** SAM **f.** PCEs distribution for the different HTM, **g.** J-V curves of the champion 1 cm^2 p-i-n PSC, **h.** J-V curves of the champion 2 cm^2 p-i-n PSC.

Table 2. Photovoltaic parameters of champion p-i-n PSCs with three different hole transport layers, Spiro-TTB, PTAA, and Meo-2PACz.

HTL	Scan direction	J_{sc} (mA/cm^2)	V_{oc} (V)	FF (%)	PCE (%)
Spiro-TTB	Reverse	22.05	1.131	81.3	20.27
	Foward	22.11	1.119	79.2	19.60
PTAA	Reverse	22.14	1.137	80.8	20.34
	Forward	22.30	1.134	80.7	20.41
MeO-2PACz	Reverse	22.30	1.121	82.4	20.61
	Forward	22.45	1.112	81.2	20.27

14

Table 3. Photovoltaic parameters of spiro-TTB based p-i-n PSCs with different active areas.

Area (cm^2)	Scan direction	J_{sc} (mA/cm^2)	V_{oc} (V)	FF (%)	PCE (%)
0.086	Reverse	22.05	1.131	81.3	20.27
	Forward	22.11	1.119	79.2	19.60
1	Reverse	22.15	1.134	76.0	19.10
	Forward	22.03	1.134	76.0	19.00
1.96	Reverse	21.95	1.131	69.4	17.19
	Forward	21.90	1.121	68.1	16.73

From all the previously discussed results, we can conclude that a controlled co-evaporation process for MAPbI$_3$ provides an effective route for the formation of a graded Fermi level across the perovskite film by affording fine-tuning of the PbI$_2$ and MAI precursors stoichiometry during the growth process. The lower Fermi levels on the bottom of the film become increasingly shallower with film thickness, resulting in a favourable energy gradient for PSCs adopting the p-i-n structure. The band bending due to changes in Fermi level is schematically shown in **Figure 4a**. The photo-generated electrons inside the perovskite are driven towards the ETL by the internal electric field, and vice versa for the holes. Therefore, p-i-n PSCs with three different HTL materials namely Poly[bis(4-phenyl) (2,4,6-trimethylphenyl) amine] (PTAA), 2,2′,7,7′-tetra (N, N-di-tolyl) amino-9,9-spiro-bifluorene (Spiro-TTB) and [2-(3,6-dimethoxy-9*H*-carbazol-9-yl) ethyl] phosphonic acid (MeO-2PACz) are fabricated with the device architecture presented in **Figure 4b**. Among these three hole-transporting materials, Spiro-TTB is useful for fully evaporated solar cells [29] while the other two have previously been shown to offer high efficiency, good stability, and potential for scalability on incorporation in PSCs [35, 64]. The PSCs based on the 3 HTL are fabricated, which exhibit PCE values consistently above 20% independently of the HTM employed. The current density–voltage (J–V) curves of the champion PSCs using spiro-TTB, PTAA, and Meo-2PACz as HTMs are reported in **Figure 4c**, **Figure 4d** and **Figure 4e**. respectively. The record PCEs achieved 20.3 %, 20.3 %, and 20.6% for spiro-TTB, PTAA, and Meo-2PACz respectively with negligible hysteresis. The photovoltaic parameters are shown in **Table 2** and **Table S5**. The internal photo conversion efficiency (IPCE) spectra and the stabilized power output (SPO) are shown in

Figure S8 for all the HTM used. The narrow PCE distribution for PSCs using the three different HTLs highlights the good reproducibility of these co-evaporated devices, **Figure 4f**. The scalability of this device architecture and the processing route is further attested by the realization of a large area PSC with an active area of 1 cm^2, PCE of 19.1%, and negligible hysteresis, **Figure 4g**. Further increase of photoactive area to 1.96 cm^2 did not lead to substantial variations of the J_{sc} and V_{oc}, **Figure 4f**, consistent with observations made in our previous studies [9, 10, 22] and the PCE reached 17.1% with neglectable hysteresis. The slight PCE decrease is driven primarily by the decrease in FF (from 81% to 69%), which is related to the increase in TCO sheet resistance (**Table 3**). [65]

Moreover, to prove the effectiveness of the graded Fermi levels towards maximization of the p-i-n PSC performance, we fabricated PSCs based on both as-deposited MAPbI$_3$ and *MAI+KAc* treated-MAPbI$_3$ [9, 22]. As previously demonstrated, the *MAI+KAc* treatment can effectively penetrate the whole film thickness and together with efficient passivation effects can also balance out the PbI$_2$ excess present, which previously allowed us to improve the photovoltaic performances of our n-i-p PSCs. [9, 22] By treating the MAPbI$_3$ films with *MAI+ KAc*, the compositional gradient is removed and the energy levels are significantly modified as verified by UPS measurements shown in **Figure S9**. Consequently, p-i-n PSCs based on both as-deposited and treated-MAPbI$_3$ show different photovoltaic characteristics. The p-i-n PSCs based on treated-MAPbI$_3$ achieved lower PCE as compared to the as-deposited sample, due to the lower FF arising from slower charge transfer at the HTL/MAPbI$_3$ and MAPbI$_3$/ETL interfaces and charge transport within the perovskite film on the removal of favourable energy band bending, as shown in **Figure S10**. The PSCs based on both as-deposited and treated-MAPbI$_3$ both show negligible hysteresis, **Figure S11**. This trend observed for p-i-n PSCs based on as-deposited and treated-MAPbI$_3$ is the opposite of what has it is observed for co-evaporated MAPbI$_3$ n-i-p PSCs both previously [9] and in this work, **Figure S12**. The n-i-p PSCs show an obvious increase across all photovoltaic parameters due to the passivating effect of potassium

ions and the removal of the unfavourable energy band bending. As expected, the graded Fermi levels in co-evaporated $MAPbI_3$ films are proved to be favorable only for PSCs adopting the p-i-n configuration.

Moreover, to further prove the benefits of the graded structures in p-i-n PSCs we have directly compared the growth condition developed in this work with another condition of perovskite growth, where the starting background pressure is consistently decreased to reduce the grading within the $MAPbI_3$. For clarity, we indicate Condition *1* when the starting pressure is 1×10^{-5} torr, while *condition 2* when the starting pressure is 4.0×10^{-6} torr, **Figure S13**. We have subsequently implemented the $MAPbI_3$ grown in both conditions in p-i-n and n-i-p PSCs to demonstrate the advantages of the two growing conditions for different device architectures. As expected, $MAPbI_3$ grown with *condition 1* is more favorable than *condition 2* to enhance the performance of p-i-n structure, **Figure S13**. On the other hand. $MAPbI_3$ grown with *condition 2*, where the gradient is not created, is more effective for n-i-p cells, **Figure S14**. These results demonstrate that different perovskite growth conditions should be applied for the different architecture of solar cells to maximize the PSCs performance.
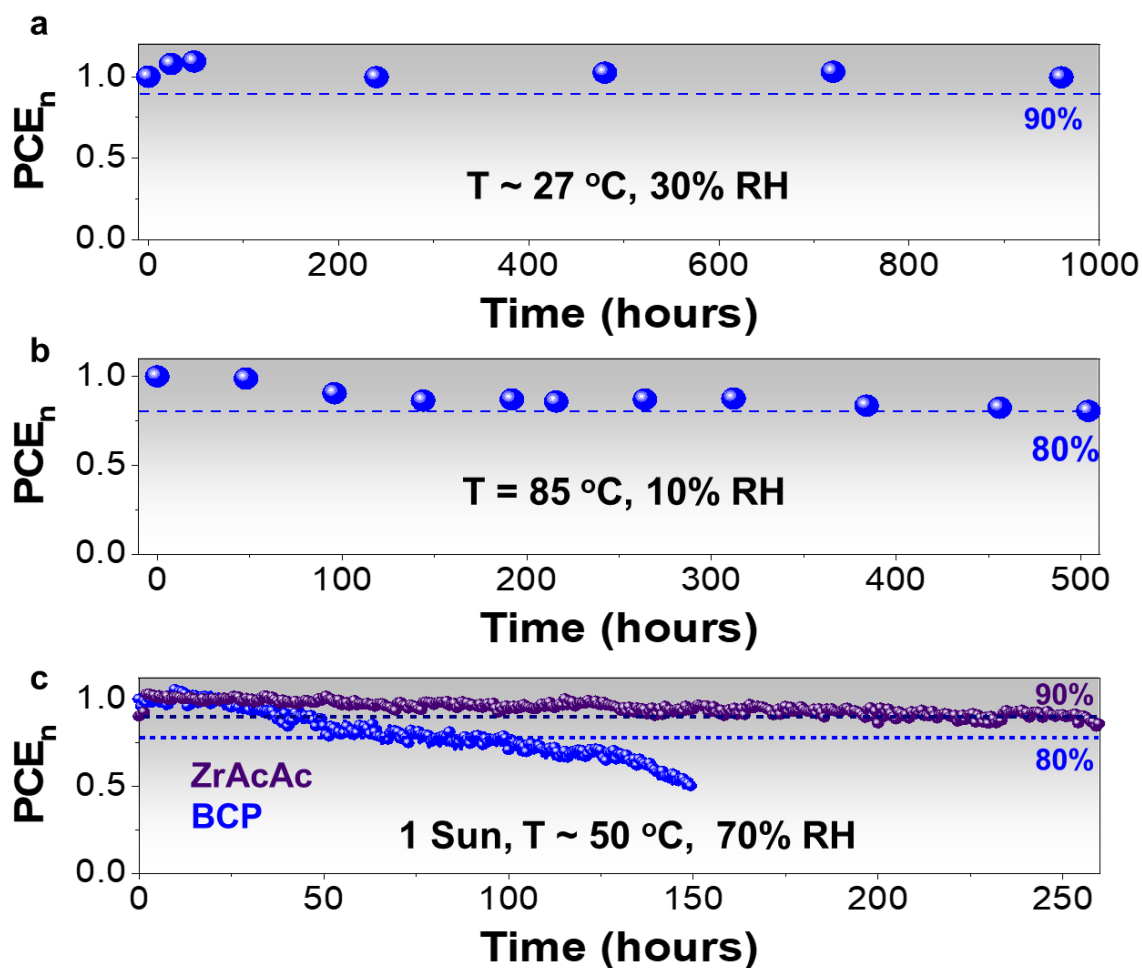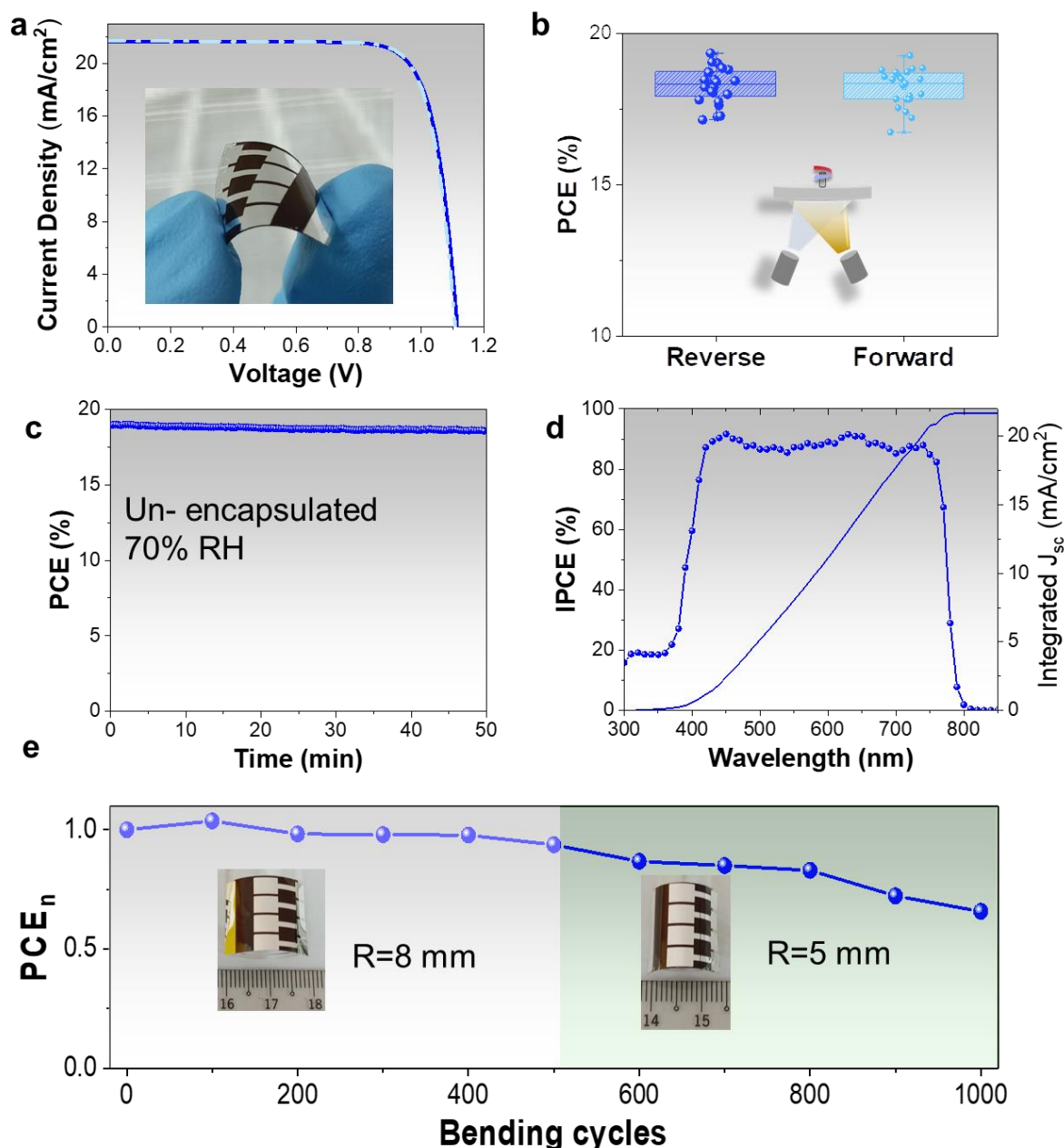
Figure 5. **Co-evaporated MAPbI₃ p-i-n PSCs long-term stability**. **a.** PCE shelf-stability as a function of time. The PSCs were stored in a controlled environment, at room temperature (~27 °C) and RH of 30%, **b.** PCE stability trend as a function of the time during continuous thermal aging at 85 °C and 10% RH, **c.** PCE stability trend as a function of time under continuous 1 Sun illumination.

These unencapsulated p-i-n PSCs also exhibit good long-term stability, with PSCs kept at room temperature and 30% RH, retaining more around 98% of their initial PCE after ~1000 hours, **Figure 5a**. The box-plot distributions of the photovoltaic parameters are shown in **Figure S15**. The p-i-n PSCs' high-temperature thermal stability has shown to be very promising; where the unencapsulated PSCs thermally aged at 85 °C and 10% RH retaining over 80% of their PCE after 500 hours, **Figure 5b**. This remarkable thermal stability for unencapsulated PSCs is in line with our previous results on n-i-p co-evaporated MAPbI₃ PSCs. [31] Moreover, the p-i-n PSCs based on Spiro-TTB as HTL and PCBM/BCP as ETL are able to retain almost 80% of their initial PCE on illumination at 1 sun (AM 1.5) for over 100 hours, in the absence of any

cooling system. The introduction of zirconium acetylacetonate (ZrAcAc) as a buffer layer of the p-i-n PSCs allows for the retention of 90% of initial PCE after 250 hours, **Figure 5c**. The complete photovoltaic characteristics of the p-i-n PCSs with ZrAcAc are presented in **Figure S16**.

Figure 6. **Flexible co-evaporated MAPbI₃ p-i-n PSCs. a.** Forward and reverse J-V curves of the champion PSC. Inset: photo of the bent flexible PSCs. **b.** PCE distributions from both forward and reverse scan; **c.** Maximum power point (MPP) MPP tracking, **d.** IPCE and integrated J_{sc} current of the flexible PSC, **e.** PCEs as a function of the bending cycles with a radius of 8 mm and 5 mm respectively.

Table 3. Photovoltaic parameters of the champion flexible p-i-n PSC.

Scan direction	V_{oc} (V)	J_{sc} (mA/cm^2)	Fill Factor (%)	PCE (%)
Reverse	1.107	21.69	80.26	19.27
Forward	1.098	21.70	81.19	19.34

As the fabrication process of these p-i-n PSCs does not require high-temperature processing, we are able to demonstrate flexible p-i-n PSCs based on the following structure: Polyethylene Naphthalate (PEN) /ITO/Spiro-TTB/MAPbI$_3$/PCBM/BCP/Ag. The champion PSC achieved a record PCE of 19.34% (**Figure 6a**, **Table 3**, and **Table S6**) with very good flexibility, **Figure 6a** inset, and negligible hysteresis for all the flexible p-i-n PSCs fabricated, **Figure 6b**. The stabilized output, on the other hand, shows PCE ~19% over 50 min at 70% RH, **Figure 6c**. The incident photon-to-current conversion efficiency (IPCE) spectrum, **Figure 6d**, reveals an integrated J_{sc} of 21.7 mA/cm^2 which is in good agreement with the value measured in the J-V scan at 0 V. The IPCE spectrum clearly shows that the lower J_{sc} achieved in flexible devices as compared to the one of PSCs on the glass substrate is due to the lower PEN transmittance substrate in the UV-visible region as reported earlier. [66] The flexible properties of the p-i-n PSCs were tested over two different bending radii, **Figure 6e**, and found to retain 90% of their initial PCE after 500 bending cycles with an 8 mm radius, and 60%, following additional 500 bending cycles with 5 mm radius.

Conclusions

In this work, we have proved the potential of the co-evaporation process in customizing the energetic properties of the perovskite layer for different p-i-n and n-i-p architectures. Specifically, we have tuned the co-evaporation process, by controlling the background pressure, to grow the MAPbI$_3$ with a gradient in composition leading to graded Fermi levels suitable for high-performing p-i-n PSCs. The same growth condition is instead not favorable for the n-i-p structure, as the Fermi levels will be opposite to the PSCs internal energy alignment.

Differently, a growth condition that minimizes the gradient inside the films guarantees better material for the MAPbI$_3$ in an n-i-p architecture, while the performances of the p-i-n PSCs are worse.

We demonstrated small area p-i-n PSCs with champion PCE of 20.6 % and consistent PCEs well above 20% for PSCs incorporating different HTLs, and larger p-i-n PSCs with 1 cm^2 and 1.96 cm^2 active areas, have shown the record PCEs values of 19.1% and 17.2% respectively. These unencapsulated co-evaporated p-i-n PSCs exhibit remarkable long-term stability, retaining 90% of their initial PCE for over 1000 hours on storage at room temperature. These p-i-n PSCs also show good thermal stability, maintaining more than 80% of their initial PCE on thermal aging at 85 ^{o}C and 10% RH, for 500 hours. Ultimately, the low-temperature processing of the p-i-n PSCs has enabled the fabrication of flexible PSCs with a PCE of 19.34%. This work validates the versatility of the thermal co-evaporation method in growing perovskite layers with energy alignments customized for different device configurations towards the development of highly efficient PSCs without introducing any extra layer or passivation process.

Experimental Section/Methods

Device fabrication
P-i-n devices: ITO substrates were etched by Zn powder and dilute HCl. The pre-etched ITO glass substrates PEN substrates were cleaned by ultrasonication in acetone, isopropanol, and ethanol for 15 minutes. Respectively.

Spiro-TTB and PTAA are dissolved in chlorobenzene with a concentration of 3 mg/ml and 2 mg/ml respectively, Meo-2PACz which was prepared according to the procedure reported earlier [64] was dissolved in isopropanol with a concentration of 0.25 mg/ml. Then the solution was dropped onto the cleaned substrates and spin-coated, For Spiro-TTB the spin speed is 4000 r.p.m., for PTAA 5000 r.p.m., for Meo-2PACz, 5000 r.p.m. for 30 seconds.

The MAPbI$_3$ perovskite film was deposited on the ITO substrates with different HTLs by using a co-evaporation deposition method. The substrates are pasted onto a rotating plate at a speed of 10 r.p.m. without temperature control (i.e., floating temperature) and the target to substrate distance is around 30 cm. The perovskite is deposited by co-evaporating PbI$_2$ powder (TCI) and MAI powder (Lumtec) in effusion sources.

The MAPbI$_3$ perovskite film was deposited on the ITO substrates with different HTLs by using the co-evaporation deposition process. The substrates are attached to a rotating plate (10 r.p.m. rotation speed) without temperature control (*i.e.*, floating temperature). The perovskite is deposited by co-evaporating PbI$_2$ powder (from TCI) and MAI powder (from Lumtec) in effusion cells. The chamber was firstly pumped down to a high vacuum condition of less than $8*10^{-6}$ Torr. Then PbI$_2$ source was heated at 260 °C and MAI at 100 °C, respectively. After MAI temperature increased to >70 °C, the chamber pressure increased to >2×10^{-5} Torr. The total deposition time was around 20 min for 100 nm film, 100 min for 400 nm film, and 180 min for 750 nm film. QCM deposition rates are not given due to the instability of the QCM readings likely caused by MAI background pressure. The films were annealed at 100 °C for 30 min.

PCBM was dissolved in chlorobenzene at a concentration of 10 mg/ml, BCP was dissolved in isopropanol at a concentration of 0.5 mg/ml. PCBM was spin-coated on the perovskite film at 1000 r.p.m. and annealed at 100 °C for 10 minutes. BCP was then dynamically spin-coated on the substrates at 4000 r.p.m. Silver was evaporated with a thickness of 100 nm to complete the device, for thermal and light stability, a gold electrode was used instead. At last, 100 nm LiF was evaporated on the glass side to work as an anti-reflection coating layer.

n-i-p devices: we followed the procedure described in our previous works [9].

Characterizations

Films

The film morphology was characterized using SEM (FESEM; JEJOL JSM-7600F). The perovskite was deposited on a glass/FTO substrate.

$MAPbI_3$ films on glass were used for the optical and X-ray diffraction measurements. The UV-vis absorption spectra and transmittance spectra were taken on a Hitachi U-3501 ultraviolet/visible/near-infrared spectrophotometer. The steady photoluminescence spectra were measured by Spectro-fluorophotometer (Shimadzu, RF-5301PC), under the excitation of a 520 nm light source with an intensity of ≈30 mW cm^{-2}.

The surface crystallinity of perovskite film was studied by grazing incidence small and wide-angle X-ray diffraction at the incident angle of 0.2 º (GIWAXS; Nanoinxider Xenocs, Cu radiation with a wavelength of 0.1541 nm). The XRD patterns of the $MAPbI_3$ films of different thicknesses were recorded using X-ray diffraction (XRD; Bruker D8 Advance XRD). The XPS spectra were recorded by an X-ray photoelectron spectroscopy (XPS; Kratos AXIS Supra XPS). Ultraviolet photoelectron spectroscopy (UPS, Kratos AXIS Supra) with He plasma at an excitation energy of 21.22 eV was used to probe the valence band and work function position of the materials. In this case, the $MAPbI_3$ films were deposited on a glass/FTO substrate

For TRMC Measurements [67], the perovskite films deposited on quartz substrates were mounted in a sealed cavity inside an N_2-filled glovebox. The TRMC technique measures the change in microwave (8–9 GHz) power on pulsed excitation of the samples at different excitation wavelengths. Neutral density filters were used to vary the intensity of the incident light. The light-induced change in microwave power is related to the change in conductance ΔG by a sensitivity factor K.[67] The rise of ΔG is limited by the width of the laser pulse (3.5 ns FWHM) and the response time of the microwave system (18 ns). The slow repetition rate of the laser of 10 Hz ensures full relaxation of all photo-induced charges to the ground state before

the next laser pulse hits the sample. Before and during the photoconductance measurements, the samples were not exposed to moisture and air to prevent degradation.

Devices

The current density–voltage (J–V) curves were measured under a simulated AM 1.5 sunlight (Newport) using a Xenon lamp. The system is calibrated by a standard silicon solar cell. The effective areas were determined by metal aperture masks of different sizes for J-V measurement. The IPCE was measured by using a PVE300 (Bentham), with a dual Xenon/quartz halogen light source in DC mode Newport Oriel Sol3A^{TM} solar simulator with a 450-watt Xenon lamp. Dark scan 1.2 V to -0.1 V. Forward scan -0.1V to 1.2V. Reverse scan 1.2 V to -0.1V. The MPP track is measured by an Autolab machine (PGSTAT302N, Software version- NOVA 1.11).

Supporting Information

Supporting Information is available from the Wiley Online Library or from the author.

Notes

Two of the authors N.M. and S.M. are directors of Prominence Photovoltaics Pte Ltd a perovskite solar cell commercialization company. The other authors have no conflict of interest to declare.

Received: ((will be filled in by the editorial staff))
Revised: ((will be filled in by the editorial staff))
Published online: ((will be filled in by the editorial staff))

References

[1]   W. Zhang, M. Anaya, G. Lozano, M. E. Calvo, M. B. Johnston, H. Miguez, H. J. Snaith, Nano Lett. **2015**, 15, 1698.
[2]   J. H. Im, C. R. Lee, J. W. Lee, S. W. Park, N. G. Park, Nanoscale **2011**, 3, 4088.
[3]   J. Chen, N. G. Park, Adv. Mater. **2018**, e1803019.
[4]   G. Xing, N. Mathews, S. Sun, S. S. Lim, Y. M. Lam, M. Gratzel, S. Mhaisalkar, T. C. Sum, Science **2013**, 342, 344.
[5]   S. D. Stranks, G. E. Eperon, G. Grancini, C. Menelaou, M. J. Alcocer, T. Leijtens, L. M. Herz, A. Petrozza, H. J. Snaith, Science **2013**, 342, 341.
[6]   Q. F. Dong, Y. J. Fang, Y. C. Shao, P. Mulligan, J. Qiu, L. Cao, J. S. Huang, Science **2015**, 347, 967.
[7]   M. M. Lee, J. Teuscher, T. Miyasaka, T. N. Murakami, H. J. Snaith, Science **2012**, 338, 643.
[8]   National Renewable Energy Laboratory. Best Research-Cell Efficiency Chart. NREL
[9]   J. Li, H. Wang, X. Y. Chin, H. A. Dewi, K. Vergeer, T. W. Goh, J. W. M. Lim, J. H. Lew, K. P. Loh, C. Soci, T. C. Sum, H. J. Bolink, N. Mathews, S. Mhaisalkar, A. Bruno, Joule **2020**, 4, 19.
[10]   J. Li, H. A. Dewi, H. Wang, J. H. Lew, N. Mathews, S. Mhaisalkar, A. Bruno, Sol. RRL **2020**, 2000473.
[11]   J. M. Ball, M. M. Lee, A. Hey, H. J. Snaith, Energy Environ. Sci. **2013**, 6, 1739.
[12]   J. Burschka, N. Pellet, S. J. Moon, R. Humphry-Baker, P. Gao, M. K. Nazeeruddin, M. Gratzel, Nature **2013**, 499, 316.
[13]   W. S. Yang, J. H. Noh, N. J. Jeon, Y. C. Kim, S. Ryu, J. Seo, S. I. Seok, Science **2015**, 348, 1234.
[14]   M. Xiao, F. Huang, W. Huang, Y. Dkhissi, Y. Zhu, J. Etheridge, A. Gray-Weale, U. Bach, Y. B. Cheng, L. Spiccia, Angew. Chem. Int. Edit. **2014**, 53, 9898.
[15]   N. J. Jeon, J. H. Noh, W. S. Yang, Y. C. Kim, S. Ryu, J. Seo, S. I. Seok, Nature **2015**, 517, 476.
[16]   F. Di Giacomo, S. Shanmugam, H. Fledderus, B. J. Bruijnaers, W. J. H. Verhees, M. S. Dorenkamper, S. C. Veenstra, W. Qiu, R. Gehlhaar, T. Merckx, T. Aernouts, R. Andriessen, Y. Galagan, Sol. Energ. Mat. Sol. C. **2018**, 181, 53.
[17]   L. Cai, L. Liang, J. Wu, B. Ding, L. Gao, B. Fan, J. Semicond. **2017**, 38, 014006.
[18]   J. H. Heo, M. H. Lee, M. H. Jang, S. H. Im, J. Mater. Chem. A **2016**, 4, 17636.
[19]   M. Yang, Z. Li, M. O. Reese, O. G. Reid, D. H. Kim, S. Siol, T. R. Klein, Y. Yan, J. J. Berry, M. F. A. M. van Hest, K. Zhu, Nat. Energy **2017**, 2, 17038.
[20]   M. Liu, M. B. Johnston, H. J. Snaith, Nature **2013**, 501, 395.
[21]   C. Momblona, L. Gil-Escrig, E. Bandiello, E. M. Hutter, M. Sessolo, K. Lederer, J. Blochwitz-Nimoth, H. J. Bolink, Energy Environ. Sci. **2016**, 9, 3456.
[22]   J. Li, H. Wang, H. A. Dewi, N. Mathews, S. Mhaisalkar, A. Bruno, Coatings **2020**, 10, 1163.
[23]   D. B. Mitzi, M. Prikas, K. Chondroudis, Chem. Mater. **1999**, 11, 542.

[24]   D. Pérez-del-Rey, P. P. Boix, M. Sessolo, A. Hadipour, H. J. Bolink, J. Phys. Chem. Lett. **2018**, 9, 1041.

[25]   M. Roß, L. Gil-Escrig, A. Al-Ashouri, P. Tockhorn, M. Jost, B. Rech, S. Albrecht, ACS Appl. Mater. Inter. **2020**.

[26]   Y.-H. Chiang, M. Anaya, S. D. Stranks, ACS Energy Lett. **2020**, 5, 2498.

[27]   L. Gil - Escrig, C. Momblona, M. G. La-Placa, P. P. Boix, M. Sessolo, H. J. Bolink, Adv. Energy Mater. **2018**, 8, 1703506.

[28]   C. Roldán-Carmona, O. Malinkiewicz, A. Soriano, G. M. Espallargas, A. Garcia, P. Reinecke, T. Kroyer, M. I. Dar, M. K. Nazeeruddin, H. J. Bolink, Energy Environ. Sci. **2014**, 7, 994.

[29]   F. Sahli, J. Werner, B. A. Kamino, M. Brauninger, R. Monnard, B. Paviet-Salomon, L. Barraud, L. Ding, J. J. Diaz Leon, D. Sacchetto, G. Cattaneo, M. Despeisse, M. Boccard, S. Nicolay, Q. Jeangros, B. Niesen, C. Ballif, Nat. Mater. **2018**, 17, 820.

[30]   D. Forgács, L. Gil-Escrig, D. Pérez-Del-Rey, C. Momblona, J. Werner, B. Niesen, C. Ballif, M. Sessolo, H. J. Bolink, Adv. Energy Mater. **2017**, 7, 1602121.

[31]   H. A. Dewi, J. Li, H. Wang, B. Chaudhary, N. Mathews, S. Mhaisalkar, A. Bruno, Adv. Funct. Mater. **2021**, 31, 2100557

[32]   E. H. Jung, N. J. Jeon, E. Y. Park, C. S. Moon, T. J. Shin, T.-Y. Yang, J. H. Noh, J. Seo, Nature **2019**, 567, 511.

[33]   M. Kim, G.-H. Kim, T. K. Lee, I. W. Choi, H. W. Choi, Y. Jo, Y. J. Yoon, J. W. Kim, J. Lee, D. Huh, Joule **2019**, 3, 2179.

[34]   Q. Jiang, Y. Zhao, X. Zhang, X. Yang, Y. Chen, Z. Chu, Q. Ye, X. Li, Z. Yin, J. You, Nat. Photonics **2019**, 1, 460.

[35]   X. Zheng, Y. Hou, C. Bao, J. Yin, F. Yuan, Z. Huang, K. Song, J. Liu, J. Troughton, N. Gasparini, Nat. Energy **2020**, 5, 131.

[36]   D. Luo, W. Yang, Z. Wang, A. Sadhanala, Q. Hu, R. Su, R. Shivanna, G. F. Trindade, J. F. Watts, Z. Xu, Science **2018**, 360, 1442.

[37]   B. Chen, J. Y. Zhengshan, S. Manzoor, S. Wang, W. Weigand, Z. Yu, G. Yang, Z. Ni, X. Dai, Z. C. Holman, Joule **2020**, 4, 850.

[38]   D. Kim, H. J. Jung, I. J. Park, B. W. Larson, S. P. Dunfield, C. Xiao, J. Kim, J. Tong, P. Boonmongkolras, S. G. Ji, Science **2020**, 368, 155.

[39]   H. Wang, J. Li, H. A. Dewi, N. Mathews, S. Mhaisalkar, A. Bruno, J. Phys. Chem. Lett. **2021**, 12, 1321.

[40]   M. Ross, L. Gil-Escrig, A. Al-Ashouri, P. Tockhorn, M. Jost, B. Rech, S. Albrecht, ACS Appl. Mater. Inter. **2020**, 12, 39261.

[41]   M. M. Tavakoli, P. Yadav, D. Prochowicz, R. Tavakoli, Sol. RRL **2020**, 2000552.

[42]   M. M. Tavakoli, R. Tavakoli, Phys. Status Solidi RRL **2020**, 2000449.

[43]   Y. Wu, X. Yang, W. Chen, Y. Yue, M. Cai, F. Xie, E. Bi, A. Islam, L. Han, Nat. Energy **2016**, 1, 1.

[44]   H. Bian, D. Bai, Z. Jin, K. Wang, L. Liang, H. Wang, J. Zhang, Q. Wang, S. F. Liu, Joule **2018**, 2, 1500.

[45]   M. Cha, P. Da, J. Wang, W. Wang, Z. Chen, F. Xiu, G. Zheng, Z.-S. Wang, J. Am. Chem. Soc. **2016**, 138, 8581.

[46]   H. W. Qiao, S. Yang, Y. Wang, X. Chen, T. Y. Wen, L. J. Tang, Q. Cheng, Y. Hou, H. Zhao, H. G. Yang, Adv. Mater. **2019**, 31, e1804217.

[47]   S. Xiong, Z. Hou, S. Zou, X. Lu, J. Yang, T. Hao, Z. Zhou, J. Xu, Y. Zeng, W. Xiao, Joule **2021**.

[48]   Q. Wang, Y. Shao, H. Xie, L. Lyu, X. Liu, Y. Gao, J. Huang, Appl. Phys. Lett. **2014**, 105, 163508.

[49]   B. Dänekamp, C. Müller, M. Sendner, P. P. Boix, M. Sessolo, R. Lovrincic, H. J. Bolink, J. Phys. Chem. Lett. **2018**, 9, 2770.

[50]   J. Lei, F. Gao, H. Wang, J. Li, J. Jiang, X. Wu, R. Gao, Z. Yang, S. Liu, Sol. Energy Mater. Sol. C. **2018**, 187, 1.

[51]   M. M. Tavakoli, P. Yadav, D. Prochowicz, R. Tavakoli, M. Saliba, J. Phys. D Appl. Phys **2019**, 52, 034005.

[52]   O. Malinkiewicz, C. Roldán-Carmona, A. Soriano, E. Bandiello, L. Camacho, M. K. Nazeeruddin, H. J. Bolink, Adv. Energy Mater. **2014**, 4, 1400345.

[53]   K. B. Lohmann, J. B. Patel, M. U. Rothmann, C. Q. Xia, R. D. J. Oliver, L. M. Herz, H. J. Snaith, M. B. Johnston, ACS Energy Lett. **2020**, 5, 710.

[54]   J. Teuscher, A. Ulianov, O. Muntener, M. Gratzel, N. Tetreault, ChemSusChem **2015**, 8, 3847.

[55]   V. Arivazhagan, J. Xie, Z. Yang, P. Hang, M. M. Parvathi, K. Xiao, C. Cui, D. Yang, X. Yu, Sol. Energy **2019**, 181, 339.

[56]   *https://gixa.ati.tuwien.ac.at/tools/penetrationdepth.xhtml*

[57]   X. Zhou, X. Li, Y. Liu, F. Huang, D. Zhong, Appl. phys. lett. **2016**, 108, 121601.

[58]   E. M. Hutter, J. J. Hofman, M. L. Petrus, M. Moes, R. D. Abellón, P. Docampo, T. J. Savenije, Adv. Energy Mater. **2017**, 7, 1602349.

[59]   J. Euvrard, O. Gunawan, D. B. Mitzi, Adv. Energy Mater. **2019**, 9, 1902706.

[60]   Z. Andaji - Garmaroudi, M. Abdi - Jalebi, D. Guo, S. Macpherson, A. Sadhanala, E. M. Tennyson, E. Ruggeri, M. Anaya, K. Galkowski, R. Shivanna, Adv. Mater. **2019**, 31, 1902374.

[61]   J. Endres, D. A. Egger, M. Kulbak, R. A. Kerner, L. Zhao, S. H. Silver, G. Hodes, B. P. Rand, D. Cahen, L. Kronik, J. Phys. Chem. Lett. **2016**, 7, 2722.

[62]   J. Liang, Z. Liu, L. Qiu, Z. Hawash, L. Meng, Z. Wu, Y. Jiang, L. K. Ono, Y. Qi, Adv. Energy Mater. **2018**, 8, 1800504.

[63]   P. Cui, D. Wei, J. Ji, H. Huang, E. Jia, S. Dou, T. Wang, W. Wang, M. Li, Nat. Energy **2019**, 4, 150.

[64]   A. Al-Ashouri, A. Magomedov, M. Roß, M. Jošt, M. Talaikis, G. Chistiakova, T. Bertram, J. A. Márquez, E. Köhnen, E. Kasparavičius, Energy Environ. Sci. **2019**, 12, 3356.

[65]   H. A. Dewi, H. Wang, J. Li, M. Thway, F. Lin, A. G. Aberle, N. Mathews, S. Mhaisalkar, A. Bruno, Energy Technol. 11, 34178.

[66]   J. Li, G. Han, K. Vergeer, H. A. Dewi, H. Wang, S. Mhaisalkar, A. Bruno, N. Mathews, ACS Appl. Energy Mater. **2019**, 3, 777.

[67]   T. J. Savenije, D. Guo, V. M. Caselli, E. M. Hutter, Adv. Energy Mater. **2020**, 1903788.

Co-evaporated MAPbI₃ with Graded Fermi Levels enables highly performing, scalable and flexible p-i-n Perovskite Solar Cells

Jia Li, Herlina Arianita Dewi, Hao Wang, Jiashang Zhao, Nidhi Tiwari, Natalia Yantara, Tadas Malinauskas, Vytautas Getautis, Tom J. Savenije, Nripan Mathews,* Subodh Mhaisalkar,* Annalisa Bruno*

We demonstrate a versatile co-evaporation approach to create perovskite layers with a gradient stoichiometry and graded energy levels energetically favourable for different devices architectures. Co-evaporated p-i-n PSCs, incorporating the customized MAPbI₃ with Graded Fermi Levels, consistently achieved power conversion efficiency (PCE) over 20% with different hole transporting layers, with champion values of 20.6%, 19.1%, and 17.2% for 0.086, 1, and 1.96 cm^2 active areas, respectively.